ISSN 1392–1207. MECHANIKA. 2020 Volume 26(5): 398–406

Simulation Studies and Experimental Verification of the Test Method for Initial Guidance Thrust

Zhuo WANG*, Tao WANG, Bo ZHANG*, Hong-wen MA***
**College of Mechanical and Electrical Engineering, Harbin Engineering University, Harbin 150001 PR China,*
E-mail: wangzhuo_heu@hrbeu.edu.cn, (Z.W.); zhangbo_heu@hrbeu.edu.cn, (B.Z.); mahongwen@hrbeu.edu.cn, (H.M)
***School of Mechanical Engineering, Hebei University of Technology, Tianjin, 300401 PR China,*
E-mail: 18846166436@hrbeu.edu.cn,(T.W.)

crossref http://dx.doi.org/10.5755/j01.mech.26.5.23460

1. Introduction

In view of the current increasingly tense international military competition, the flight performance of the missile needs higher requirements. The electric steering gear is the main actuator in the process of the missile guidance, whose performance parameters largely determine the accuracy and stability of the missile guidance system [1-4]. In order to improve the accuracy of the missile during the flight, it is very important to analyze and study the test mechanism of the initial pilot jet thrust of the electric steering gear and perform the corresponding experimental research.

At present, most of the existing jet thrust test systems at home and abroad, adopt the indirect measurement method [5]. Indirect measurement method considers the system in the process of loss of transmission and other factors. In contrast, the direct measurement method offers a higher accuracy, however, is not widely used due to the difficulty of analyzing the jet flow field [6-8]. When the jet impinges directly on the bearing wall, the jet flow field can be regarded as turbulent impinging flow field. Over the years, many scholars at home and abroad have studied the turbulent impact and made significant contributions in the study of the mechanism of jet thrust test [9, 10].

In 2001, Fairweather M. and Hargrave G. K. [11] observed the flow field by particle image velocimetry to obtain the average jet velocity and shear stress of air jets incident on a flat surface. In 2005, JW Hall and D Ewing [12] at the McMaster University in Hamilton studied multiple fluctuating wall pressures on wall jets formed by different Reynolds number jets to study the simulation of radial wall jet near field large eddy structure changes. Z Xu and H Hangan et al. (2008) [13] studied the sensitivity of the orthogonal impinging jet on the Reynolds number, boundary conditions (geometry and surface roughness), and inlet conditions. It was found that when the impinging jet reached the full roughness region, the depth of the surface layer increased with an increase in the roughness.

Tummers M.J, Jacobse J and Voorbrood S.G.J et al. (2011) [14] exhaustively studied the turbulence in the stagnant area of a single impinging jet pipe. In 2015, Kalifa RB, Habli S, Said NM et al. [15] studied the flow field formed by a planar air jet impact on a flat surface using the Reynolds number average equation and RSM second-order turbulence closure. The model was studied using the computational fluid dynamics. The results obtained at the end quantified the effect of the flow distortion on the turbulent structure of a complex three-dimensional impingement flow.

To date, most reports on the turbulent impinging flow field were studied by using the flow field analysis and an experimental verification, and on the basis of it, the turbulent structure inside the turbulent flow field was obtained. However, the bearing force of the bearing wall under impinging jet under different conditions has not been extensively studied. In this pursuit, the present research envisaged the study of influence of different bearing wall positions on the wall pressure, and based on the analysis of the flow field simulation, optimization of the bearing wall structure was done.

2. Analysis method of flow field in jet thrust test

2.1. Analysis of flow field in jet thrust test

The initial guidance thrust flow field has typical hydrodynamic characteristics in practice. Many scholars at home and abroad have studied the flow characteristics of impinging jets in a single-phase flow system and found that the impinging jets can be divided into a free jet zone, an impingement zone, and a wall jet zone [16-18].

The Planter boundary layer equation in the impinging jet flow field is:

$$\rho \frac{\partial}{\partial x} \int_0^{\delta} (w_0 - w_x) w_x dy = \tau_s + \delta \frac{\partial p}{\partial x}. \tag{1}$$

From the Plant hypothesis available in the wall velocity distribution:

$$\frac{w_x}{w_0} = \left(\frac{y}{\delta} \right)^{1/7}. \tag{2}$$

Substituting Eq. (2) into Eq. (1) yields:

$$\int_0^{\delta} (w_0 - w_x) w_x dy = \frac{7}{72} w_0^2 \delta. \tag{3}$$

Since p represents the pressure difference between the two sides of the microelement, the order of $\delta dp/dx$ magnitude is too small and can be neglected in the calculation. Therefore, the surface viscous stress can be simplified as follows:

$$\tau_s = \rho \frac{d}{dx}\int_0^{\delta}(w_0 - w_x)w_x dy - d\frac{dp}{dx} = \frac{7}{72}\rho {w_0}^2 \frac{d\delta}{dx}. \quad (4)$$

The relationship between the surface stress τ_s and the thickness of the boundary layer δ can be derived from the Platts' empirical formula as follows:

$$\frac{\tau_s}{\rho {w_0}^2} = 0.023\left(\frac{w_0\rho\delta}{\mu}\right)^{-\frac{1}{4}}. \quad (5)$$

Substituting Eq. (5) into Eq. (6):

$$\delta = 0.377\frac{w_0 x}{\mu}^{-\frac{1}{5}}. \quad (6)$$

Finally, Substituting Eq. (6) into Eq. (4), the value of τ_s can be obtained:

$$\tau_s = 0.0294\rho {w_0}^2\left(\frac{w_0 x}{\mu}\right)^{-\frac{1}{5}}. \quad (7)$$

Therefore, the total stress of one side wall in the boundary layer can be calculated by an integral as:

$$F = b\int_{L_0}^{L}\tau_s dx = 0.0368 b\rho {w_0}^2\left(L^{\frac{4}{5}} - {L_0}^{\frac{4}{5}}\right)\left(\frac{w_0}{\mu}\right)^{-\frac{1}{5}}. \quad (8)$$

It can be seen from the above Eq. (8) that the accumulated viscous stress is proportional to the distance from the bearing plate when the stress is satisfied, the cumulative stress is smaller. Moreover, the cumulative stress is positively correlated with the plate thickness. However, compared with the length of the bearing plate, the variation of the thickness has a greater impact on the accumulated stress.

Finally, from the overall consideration, the installation size of the piezoelectric sensor consisted the plate length of 30 mm, a width of 20 mm, and a thickness of 5 mm.

In order to make the turbulence model more suitable for the calculation of the impinging flow field, the simulation parameters of the model were modified [19, 20]. In this paper, mainly by correcting the eddy viscosity coefficient, we determined its role in the correction of the model.

Initially, the curvilinear coordinate system (ζ_1, ζ_2, ζ_3) was established along the circumferential, radial and streamline direction of the flow field in the impinging flow field due to the radial acceleration of the flow field line direction, the radial Additional Reynolds stress, denoted as $E_{\zeta 2}$ and the influential term of curvature of the flow field, denoted as $E_{\zeta 3}$.

Curvilinear coordinate system conversion equations are as follows:

$$\xi_1 = \xi_1(x, y, z), \quad (9\ a)$$

$$\xi_2 = \xi_2(x, y, z), \quad (9\ b)$$

$$\xi_3 = \xi_3(x, y, z). \quad (9\ c)$$

The effects of additional Reynolds stress and streamline curvature on the radial of the flow field are as follows:

$$E_{\xi 2} = \frac{9}{4}\left(-4\rho\omega_3\overline{u_{\xi 2}' u_{\xi 1}'}\right), \quad (10)$$

$$E_{\xi 3} = \frac{9}{4}\left(-4\rho\frac{U_{\xi 3}}{R_{\xi 3}}\overline{U_{\xi 3}U_{R\xi 3}}\right). \quad (11)$$

In this impinging jet flow field, the circumferential strain rate is negligible because it is relatively small in magnitude compared to other quantities.

In the established flow field curve coordinate system, the average velocity can be expressed as:

$$\begin{bmatrix} U_{\xi_1} \\ U_{\xi_2} \\ U_{\xi_3} \end{bmatrix} = \begin{bmatrix} \xi_{1,x}U_1 + \xi_{1,y}U_2 + \xi_{1,z}U_3 \\ \xi_{2,x}U_1 + \xi_{2,y}U_2 + \xi_{2,z}U_3 \\ \xi_{3,x}U_1 + \xi_{3,y}U_2 + \xi_{3,z}U_3 \end{bmatrix}. \quad (12)$$

The transformation matrix form is:

$$\begin{bmatrix} U_{\xi_1} \\ U_{\xi_2} \\ U_{\xi_3} \end{bmatrix} = \begin{bmatrix} \xi_{1,x}\ \xi_{1,y}\ \xi_{1,z} \\ \xi_{2,x}\ \xi_{2,y}\ \xi_{2,z} \\ \xi_{3,x}\ \xi_{3,y}\ \xi_{3,z} \end{bmatrix}\begin{bmatrix} U_1 \\ U_2 \\ U_3 \end{bmatrix}. \quad (13)$$

The impulsive dissipation term ε in the impinging jet flow field represents the degree of turbulent kinetic energy transfer from the large eddy to the small eddy. In the curved flow field coordinate system, the fluctuating kinetic energy equation and the loss rate can be obtained as follows:

$$\frac{\partial(\rho k)}{\partial t} + \nabla\bullet(\rho U_{\xi i}k) = \nabla\bullet\left[\left(\mu + \frac{\mu_t}{\sigma_k}\right)\nabla k\right] + \\ + P_k - \rho\varepsilon, \quad (14)$$

$$\frac{\partial(\rho\varepsilon)}{\partial t} + \nabla\bullet(\rho U_{\xi i}\varepsilon) = \left(\mu + \frac{\mu_t}{\sigma_\varepsilon}\right)\nabla\varepsilon\bullet\nabla + \\ + \frac{\varepsilon}{k}\left[C_{\varepsilon 1}P_k - C_{\varepsilon 2}\rho\varepsilon\right]. \quad (15)$$

In formula: $E_k = E_{\zeta 2} + E_{\zeta 3}$, eddy viscosity $\mu_t = \rho C_u k^2/\varepsilon$. The coefficients of the turbulence model are μ_t=0.085, σ_k=1, σ_ε=1.3, $C_{\varepsilon 1}$=1.44, and $C_{\varepsilon 2}$=1.88.

It can be seen from the above equations that the eddy viscosity in the *k*-ε model can be obtained by the Eq. (15), and the coefficient C_u is approximately 0.085. But in the actual bending flow field, the eddy viscosity μ_t related to it should not be constant, since the ratio of radial pulsation velocity and k is not constant in the solution area.

Ni Hangen et al. made assumptions and derived the Cu solution from the turbulence modelling control equations, and were able to reflect the changes in $\mu_{t,,}$ as follows:

$$C = \alpha \Big/ \left\{1 + \alpha\left[\frac{k}{\varepsilon}\left(\frac{\partial u}{\partial y} + \frac{\partial v}{\partial x}\right)\right]\right\}. \quad (16)$$

According to the experimental data of the existing turbulent boundary layer by least squares fitting, the constants were found to be: $\alpha_1 = 0.254$ and $\alpha_2 = 0.132$.

Values of k and ε can be calculated by Eq. (17) and Eq. (18), and can be used to correct the standard k-ε equation, when the initial model conditions are set in the flow field simulation analysis.

When the impact jet nozzle diameter D is 5 mm, the first guide thrust test provides a flow of 20 m/s velocity of the compressed gas, the radial average velocity at the exit of the impinging jet is 0, the average velocity in the axial direction is 20 m/s, the C_u gas is 0.085, the kinematic viscosity of air is μ=14.8×10^{-6} m^2/s, then by the formula $v_0=V_j=Re\cdot\mu/d$, the value of Re can be found as: Re=6900.

Other model coefficients k, ε are given by:

$$k = 0.0036V_j^2 = 1.2, \tag{17}$$

$$\varepsilon = \frac{C_\mu^{3/4}k^{3/2}}{0.07d/2} = 7.8\times10^4. \tag{18}$$

Therefore, the corrected C_u value can be obtained from Eq. (18) as 0.254, and the flow field model can be corrected by using the obtained turbulence model coefficients in the thrust test flow field simulation.

2.2. Flow field simulation analysis of jet thrust test

The operating environment and the operating pressure were set, the relative pressure was equal to absolute pressure, and the impact of gravity was not considered. The bearing surface material was selected to be stainless steel SS-304, since it is a solid material, and in the simulation of unsteady turbulent flow field, a constant density, thermal conductivity and specific heat capacity of the material is necessary [21].

After setting the initial conditions, the flow field of the impinging jet was numerically simulated using the fluent software. By analysing the change in the annular recirculation zone in the flow field, the relationship between the impingement distance H and the flow field line was obtained, and the optimal impact position was obtained.

As the flow field in the actual situation is more complicated, the flow field model was simplified. As shown in the Fig.1, the inlet boundary diameter D was set to 5 mm. taking into account the actual experimental space, value of H/D was selected as 3, 4, 5, 6, 8, and 10 in the simulation analysis.

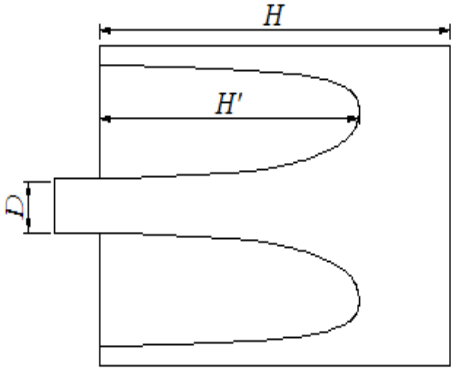

Fig. 1 Entrance and exit boundaries

When the velocity of inlet impact flow was 20 m/s, equal to that of different impact height (H/D = 3, 4, 5, 6, 8, 10), a flow was obtained by simulating the modified two-field map, as shown in Figs. 2 a - f. In Fig. 2, the flow field line is the movement path of the gas in the flow field. The colour of the flow field line indicates the velocity in the direction perpendicular to the bearing wall. Due to the existence of the bearing wall surface, when the velocity in the normal direction to the wall surface was zero, field lines completely changed the maximum wall pressure.

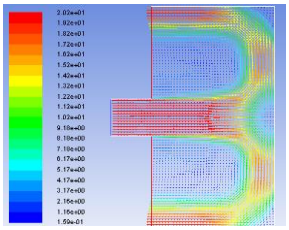

a) H/D= 3speed vector

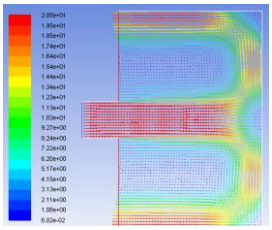

b) H/D=4speed vector

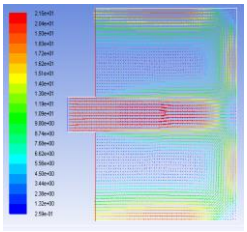

c) H/D= 5speed vector

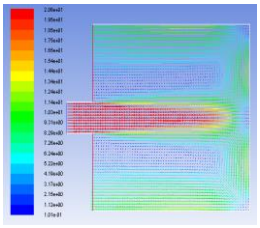

d) H/D= 6speed vector

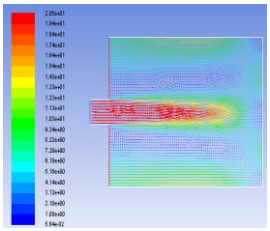

e) H/D=8speed vector

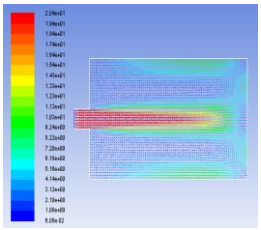

f)H/D=10speed vector

Fig. 2 Different H/D ratio of the flow field in the circumfluence map

It can be seen from Fig. 2 that the annular recirculation zone was formed at different impact heights H, where we consider the relative ratio of the height at the transition of the annular recirculation zone to the impact height H. The plot of the relative position of the annular recirculation zone under different H/D curves is shown in Fig. 3. A variation in the annular recirculation zone with the change of H/D value was obtained through the fitting optimization, as shown in Fig.3.

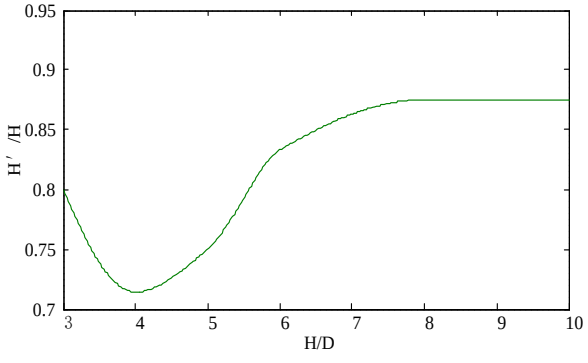

Fig. 3 Flow field loop is backflow area curve

It can be seen from the Fig. 3 that when the distance *H* between the bearing wall and the spout increased from 3*D* to 8*D*, the relative position of the centre of the annular recirculation zone changed greatly, and the relative position tended to be stable when the *H* value was greater than 8*D*. The smaller the relative position value was, the farther was the recirculation zone. Different recirculation zone positions led to different size and position of the core region of the impinging jet, thereby affecting the position of the stagnation point and the range of the impact zone.

Considering the accuracy of the initial guidance test during the test, the initial choice of *H/D* = 4 for found to be the best bearing wall position, and the wall pressure analysis further verified that the selected value of H was accurate. Fig. 4 was obtained after simulating the flow field under different impact height (*H/D* = 3, 4, 5, 6, 8, 10) to obtain the pressure distribution at the bearing wall surface.

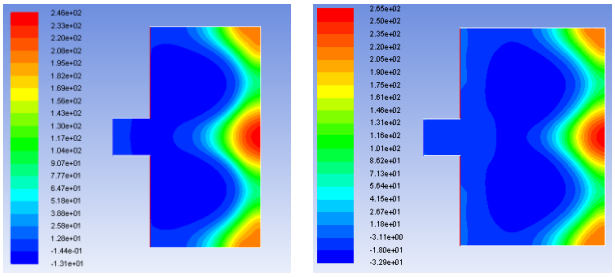

a) *H/D*=3 pressure diagram b) *H/D*=4 pressure diagram

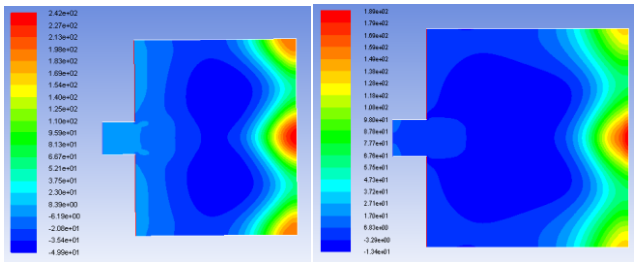

c) *H/D*=5 pressure diagram d) *H/D*=6 pressure diagram

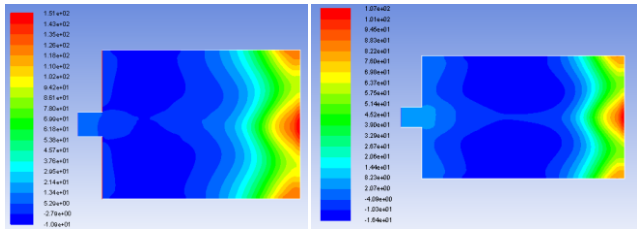

e) *H/D*=8 pressure diagram f) *H/D*=10 pressure diagram

Fig. 4 Different *H/D* ratio of the bearing wall pressure chart

It can be seen from the Fig. 5 that with a change in the value of *H/D*, the bearing wall pressure was not linear, but initially increased and subsequently decreased, for an *H/D* value of 3 to 5. For the *H/D* value of 4, a maximum wall centre pressure of 265 N was obtained. Through the simulation, the stress distribution on the test bearing wall was compared with the distribution of the recirculation zone, under the different *H/D* conditions in the previous study. The two showed a good agreement with each other, and the simulation is for reference. Finally, *H/D* = 4 was selected for the placement of the best place tablet. However, it should be noted that this study is only a preliminary simulation analysis for obtaining the *H/D* values. The continued optimization of its value needs a further study.

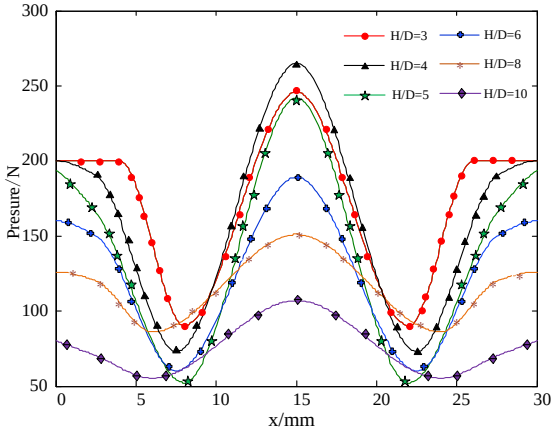

Fig. 5 Pressure curves at different *H/D* values

2.3. Selection and analysis of impact wall structure

Through the analysis of the upper section, it can be seen that the wall position is reasonable when the impact wall surface *H/D* is taken as 4. Since the flat wall surface is the most common wall structure, in order to analyse the influence of different bearing wall structures on the thrust test, the wall surface optimization design is now carried out. We selected U-shaped groove, V-shaped groove and square groove for simulation analysis and observation, these are shown in Figs.6, a – c. The flow field diagram of the three type are shown in Figs.7, a – c).

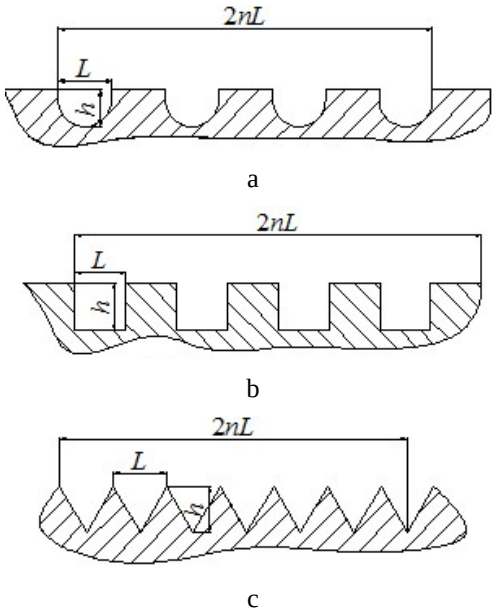

Fig. 6 a) U-shaped groove; b) square – shaped groove; c) V – shaped groove

In Figs. 6, a – c, the depth of groove *h* is 0.4*D*, the length of groove *L* is 0.5*D*, the number of grooves *n* is (15~20) *D*.

By calculation, the U-shaped groove, the V-shaped groove, and the square groove have $H^{'}/H$ values of 0.650, 0.658, and 0.698 when the inlet boundary condition is set to 20 m/s. From the obtained values, the relative position of the jet recirculation zone of the square groove wall surface is closer to the wall surface, and the difference between the U-shaped groove and the V-shaped groove is smaller. Through the Fluent simulation analysis, the wall pressure of the three

walls is further analysed. The specific pressure cloud diagram is shown in Figs. 8, a – c.

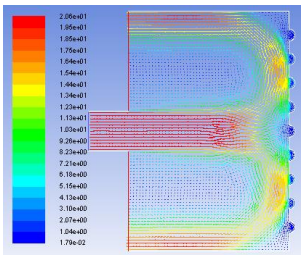

a) Flow field streamline under U-shaped groove

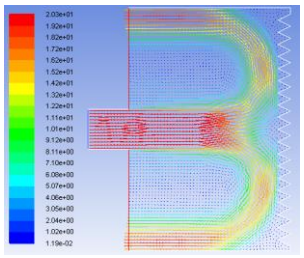

b) Flow field streamline under V-shaped groove

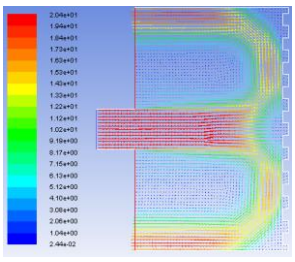

c) Flow field streamline under square slot

Fig. 7 Fluid speed vector under various type of trough

After obtaining the pressure cloud map by simulation, it can be seen from Fig. 8 that the distribution trend of impact pressure on the three walls is similar, the main difference is the range of the impact zone and the uniform pressure of the wall zone. After the post-treatment, the bearing wall pressure curve is shown in Fig. 9.

It can be seen from the above Fig.9 that when the three types of channel wall surface are *H*/*D*=4, the maximum pressure value of the square groove wall surface is

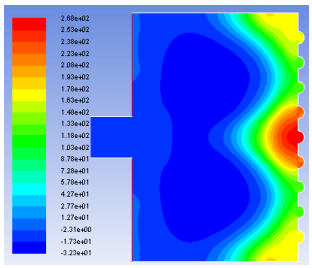

a) Pressure on U-shaped groove wall

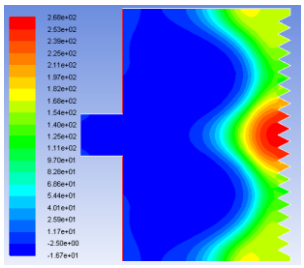

b) Pressure on V-shaped groove wall

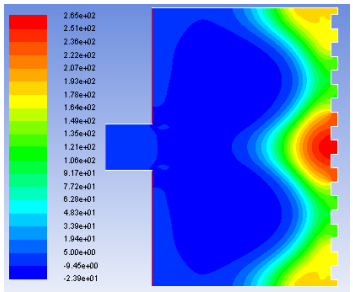

c) Pressure on square shaped groove wall

Fig. 8 Pressure on three types of groove wall

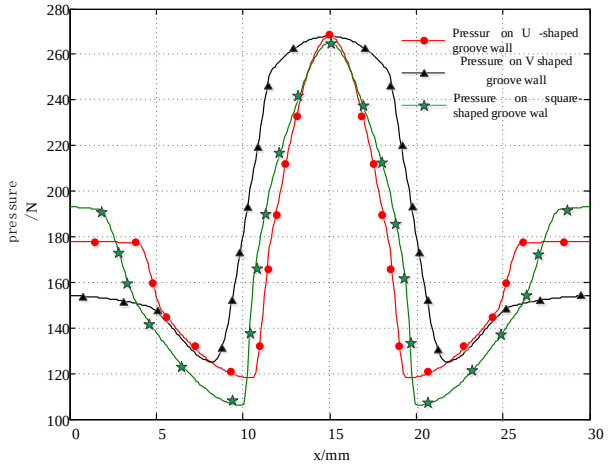

Fig. 9 Pressure curve on three types of groove bearing wall

small, which is 265 N; the maximum pressure values of the U-shaped groove and the V-shaped groove wall surface are similar, both being 268 N. It can be seen from the peak of the curve that the impact zone range of the V-shaped groove wall surface is larger than that of the U-shaped groove wall surface. When the impact area is larger, the pulsation point pressure of the wall surface is closer to the surface pressure, and the thrust value obtained by the test is close to the true value. Therefore, the V-shaped groove is selected as the optimized wall surface.

3. Design of initial guidance thrust test device

The study of the structure scheme of the initial guidance thrust test system was specifically designed considering the force transmission mode and the fixed mode of the electric steering gear during the jet thrust test.

In the existing thrust test device, most of its thrust force was transmitted to the load cell through the connecting elastic member, and a certain loss of face value occurred in the process, so that the sensitivity of the test was reduced. Therefore, the direct measurement method was adopted. The thrust force acted on the bearing wall to deform the piezoelectric sensor, and finally the measured thrust value was obtained, and from the optimisation of the air jet flow field, the measurement position simulation was done analysis to improve the thrust test accuracy.

The primary guidance thrust test can be divided into static thrust test and dynamic thrust test. The so-called static thrust test is the thrust test of the electric servo, in which the rudder wing is fixed by the clamping device. As the electric servo has its own internal positioning, it only needs a unilateral clamping, and to a certain extent it optimizes the overall size of the test system. Unlike static tests, the dynamic thrust test turns the rudder wings in a free-wheeling condition during jet thrust testing of the electric servos.

Initially, the static thrust test was structurally designed as showed in Fig. 10.

In the working of the thrust test device, first by rotating the clamping part of the rotary handle *9*, the clamping jaw *8* was clamped with the servo wing under by 0°. After the completion of the servo wing clamping action, by turn-

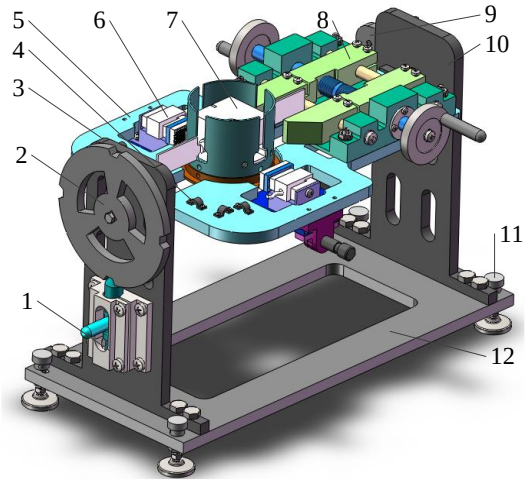

1 – lock mechanism; *2* – position turn plate; *3* – left support plate; *4* – cable block; *5* – support plate; *6* – slide sensor; *7* – the rudder wing fixed positioning mechanism; *8* – the clamping jaw; *9* – flip platform rotary handle; *10* – right support plate; *11* – horizontal adjustment foot; *12* – base and other components

Fig. 10 Static thrust test diagram

ing the rotary handle *9*, the support plate *5* was turned to 180° rotations, so as to facilitate the adjustment of the following components and installation.

The inverted position was determined by the pin at lock mechanism *1*. Since the pin gets worn due to repeated use, an anti-backlash structure was adjusted by screwing. After the installation was complete, the initial guide thrust force obtained by the piezoelectric sensor *6* could be clearly seen from the output value of the cable connected to the computer. In order to ensure that the sensor centre and the servo outlet were in the same axis in the initial guidance static thrust measurement process, the specific installation parts are shown in Fig. 11, a, b.

The difference in the dynamic and static thrust test was mainly reflected by the position of the rudder wing, as shown in Fig. 12.

In the dynamic thrust test, positioning the rudder wing was not required. In order to balance the influence of the rudder wing on the overall mechanism during the swinging process, the overall structure was centre-symmetrical.

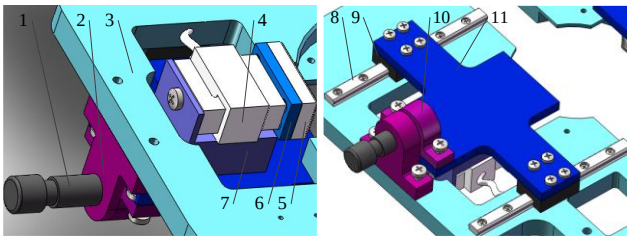

a) Top view b) Bottom view

1 – screw; *2* – screw drive left bracket; *3* – support base plate; *4* – piezoelectric sensor; *5* – load plate; *6* – connector; *7* – sensor base; *8* – guide rail; *9* – slider; *10* – screw drive right bracket; *11* – moving bottom plate

Fig. 11 Static sensor installation diagram

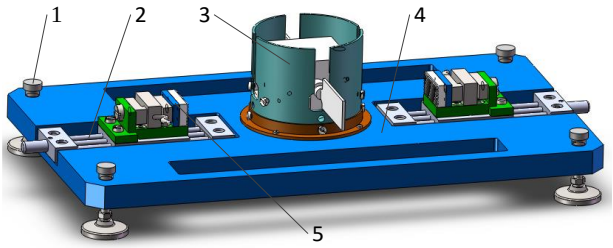

1 – slide mechanism; *2* – steering positioning components; *3* – base; *4* – sensors; *5* – level adjustment feet

Fig. 12 Dynamic thrust test diagram

4. Thrust test simplifies the experiment

4.1. The initial guidance thrust test system

The initial guidance thrust test system mainly consisted of a gas source station, a static thrust test device, a dynamic thrust test device and an electronically controlled part. The static and dynamic test device are shown in Figs. 13 and 14.

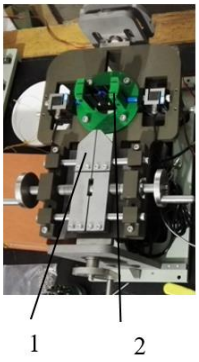

1 – the static thrust test device; *2* – the pneumatic base

Fig. 13 Static test device

1 – the dynamic thrust test device; *2* – the pneumatic base

Fig. 14 Dynamic test device

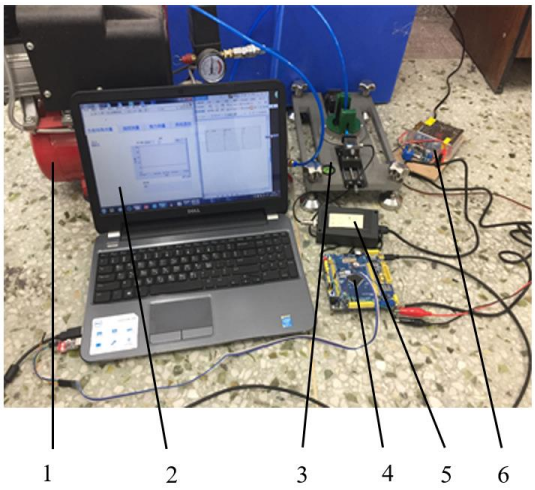

Fig. 15 Simplified thrust test experimental scheme

Due to the limitation of experimental conditions, it was not possible to provide the electric steering gear, steering gear cabin and the impact jet at the speed of 20 m/s, in the actual initial pilot thrust test. Therefore, only simplified experiments can verify the simulation of the optimal wall

position proposed in the analysis of whether the *H*/*D* value is 4 or not. Because the testing mechanism was consistent, this test simplified the dynamic thrust test device [22]. The simplified test principle is shown in Fig. 15. This experimental test device was mainly composed of air pump *1*, computer display interface *2*, static force test device *3*, single chip acquisition system *4*, transmitter *5*, and power supply *6*.

4.2. Selection of main components

1. Rotary potentiometer.

An angle sensor is required in the load table to monitor the corner of the rudder wing during the test in real time. According to the technical requirements of the load platform, the rotating point device type of WDD35D-1 is selected. The actual object is shown in Fig.16.

Fig. 16 The type of WDD35D-1 rotary potentiometer

The specific performance parameters are shown in Table 1.

Table 1

Rotary potentiometer performance parameters

Elements	Parameters index
Resistance	0.5～10KΩ
Resistance tolerance	±15%
Independent linearity	0.1%
Operating temperature	-55℃～125℃
Mechanical corner	360°
power	2W

2. Piezoelectric sensor.

The piezoelectric sensor is the main detection component in the initial guided thrust test system, which can satisfy better dynamic characteristics. The signal acquisition performance of the piezoelectric sensor will directly affect the measurement accuracy of the initial guided thrust test device. According to the performance index requirements, the type of NOS-L101 sensor is selected, as shown in Fig. 17.

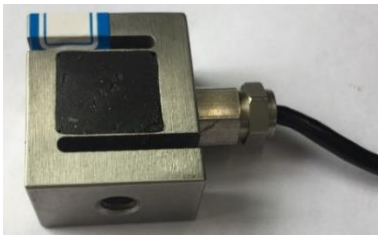

Fig. 17 NOS-L101 model sensor

The specific performance indicators of the selected piezoelectric sensors are shown in Table 2.

Table 2

Piezoelectric sensor performance parameters

Elements	Parameters index
Sensitivity	2.0mv/V
Sensitivity temperature effect	±0.02%F·S/10 ℃
Creep	±0.02%F·S/30min
Zero output	±1%F·S
Zero temperature effect	±0.02%F·S/10 ℃
Temperature compensation range	–10～+40 ℃
Operating temperature range	–20～+65 ℃
Excitation voltage	5～12VDC
Safety overload range	150%F·S

3. Transmitter.

After selecting the above NOS-L101 piezoelectric sensor, we selected the transmitter with the matching model N0S-TDA for signal processing. The main function of the transmitter is to amplify the tiny millivolt electrical signal output by the piezoelectric sensor, and perform linear compensation and temperature compensation through its internal voltage regulation processing, as shown in Fig. 18.

Fig. 18 Transmitter products

The specific performance indicators of the transmitter are shown in Table 3.

Table 3

Transmitter specific indicators

Elements	Parameters index
Input form	Single input and single output
Rated input	0～20V
Rated output	0～5V or 0～10V
Precision	≤±0.05～0.1
Supply voltage	24VDC
Operating temperature	–20～+85 ℃

4.3. Test process and analysis

The gas source of the simplified experimental device was provided by a 0.8 MPa pressure pump, the airflow was provided as an output to a dynamic jet thrust test device through a sleeve connector with a diameter of 6 mm, an air pump and a test device were connected through a hose, and the output voltage of the piezoelectric sensor was kept at 5 V. The full-scale force value of 5 N in the first calibration of the sensor through the calibration device is shown in

Fig. 19. This device included the components such as weights *1*, trays *2*, transmitters *3*, multi-meter *4*, and power supplies *5*.

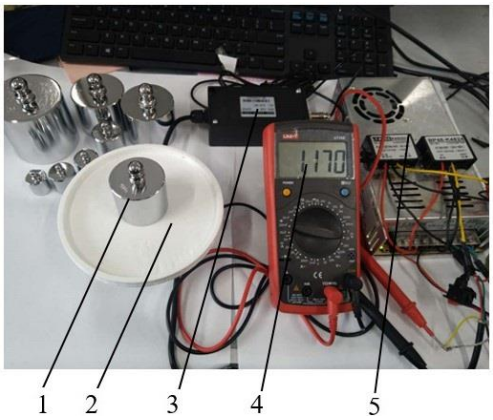

Fig. 19 Piezoelectric sensor calibration device

After the calibration of the piezoelectric sensor was completed, the thrust test was carried out. As it was a simple test, the air pressure provided by the air pump was small at 0.6 MPa and the jet outlet aperture was 6 mm. The resulting thrust value and its corresponding *H/D* value are plotted in Table 4.

Table 4

Thrust test experimental data

Serial number	*H*, mm	*H/D*	Pressure, N
1	6	1.00	3.19
2	7	1.16	3.0
3	8	1.33	2.88
4	10	1.66	2.85
5	13	2.17	2.80
6	15	2.50	2.77
7	18	3.00	2.78
8	20	3.33	2.70
9	25	4.16	2.93
10	30	5.00	2.67
11	35	5.83	2.65
12	40	6.67	2.55
13	45	7.5	2.47
14	50	8.33	2.36
15	55	9.17	2.29

The relationship between the *H/D* value obtained in this case and the corresponding pressure and the pressure value to which the distance *H* and the bearing wall surface were subjected are respectively plotted in Figs. 20, a and b.

It can be seen from Fig. 20 that, when the *H/D* value increased in proportion to *H*, the corresponding pressure value first reached a peak value of 3.19 N at about *H/D* value of 1, which was the peak value The reason is that the wall of the bearing wall was too close to the jet outlet, as result, the secondary reflow phenomenon occurred. The pressure peak was not the true value, so the second peak was observed. When the *H/D* value was about 4.16, the bearing wall pressure reached a second peak at 2.93 N. The value of *H/D* at the second peak was close to that of the previous simulation, which verified the accuracy of the previous simulation.

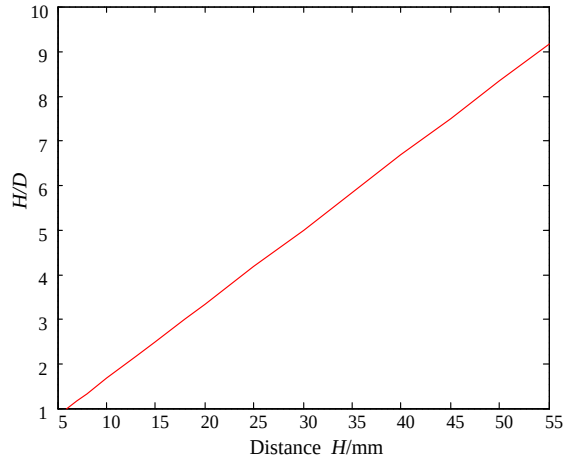

a) Distance *H* and *H/D* value diagram

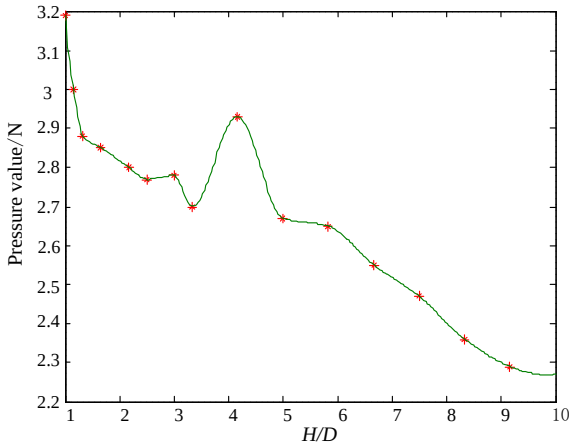

b) *H/D* value and pressure value diagram

Fig. 20 Relationship between *H*, *H/D* and pressure values

5. Conclusion

This paper focused on the analysis of the jet thrust test mechanism and the optimal distance of the bearing wall from the jet outlet. Based on this aspect, an initial pilot jet thrust test device for electric steering gear based on direct thrust measurement was proposed. The simulation results showed that the optimum distance of the bearing wall was *H/D* = 4 for jet thrust test, and a prototype test was performed to provide a preliminary verification of the accuracy of the simulation results.

Acknowledgments

his paper is funded by NSFC (Contract name: Research on ultimate bearing capacity and parametric design for the grouted clamps strengthening the partially damaged structure of jacket pipes). (Grant No: 51879063) and (Contract name: Research on analysis and experiments of gripping and bearing mechanism for large-scale holding and lifting tools on ocean foundation piles), (Grant No: 51479043). The views expressed here are the authors alone.

References

1. **Bauer, P.; Sitar, J**. 2006. Evaluation of electromagnetic actuator analysis. Power Electronics Specialists Conference, Pesc '06. IEEE:1-6.

2. **Sha, N. S.; Li, J.** 2004. A study of power-transfer-airborne integrated electric actuation system, Journal of Beijing University of aeronautics and A 30(9): 909-912 (in China).
3. **Li, Y. M.** 2012.Helicopter parallel servo automatic test system design, Harbin Institute of Technology, p. 56-68 (in China).
4. **Lu, J.; Zhang, Y. G.; Wang, C. L.** 2010. An overview of the technology of electric servo redundancy, Journal of Mechanical Transmission 34(3): 92-95 (in China).
5. **Parvezi, I,; Aris, I.; Norhisam, M.** 2011. Thrust analysis and measurement of a tubular linear permanent magnet motor in spray application (Asia-Pacific Symposium on Applied Electromagnetics and Mechanics (APSAEM10)), Journal of the Japan Society of Applied Electromag-netics 19(3): S83-S86.
6. **Shi, K. Y.; Chen, Q.; Li, H. B.** 2017. A thrust optimization method for attitude control engine, Modern Defense Technology 45(1): 12-18 (in China).
7. **Liu, X. H.; Yang, F. H.; Wei, Y. M.; Chen, J.; Wang, X. D.; Mao, W.; Li, F.; Yu, X. L.** 2017. Study on dynamic thrust test method based on torsion-swing bench, Propagation Technology 38(4): 925-931 (in China).
8. **Xia, H. W.; Ma, G. C.; Wang, C. H.** 2017. A multidimensional continuous jet thrust device for spacecraft ground simulation, CN 106644369 B (in China).
9. **Chen, Q. G.; Xu, Z.; Wu, Y. L.,Zhang Y. J., Zhang Y. C.** 2005. PIV experimental study of turbulent impinging jets in rectangular tube, Strial Fluid Mechanics 19 (1): 87-93 (in China).
10. **Yuan, D.; Wang, B. X.; Wang, Z. D., Wu, D.** 2016. Numerical simulation of impingement jets with single nozzle, Innovative ideas, young pioneers, Chinese Society for Metals Young Scholar (in China).
11. **Knowles, K.; Myszko, M.** 1998. Turbulence measurements in radial wall-jets, Experimental Thermal & Fluid Science 17(1–2): 71-78.
12. **Fairweather, M.; Hargrave, G. K.** 2001. DPIV Measurements in Axisymmetric, Impinging Turbulent Jets, DLR-Mitteilung (3):707-713.
13. **Hall, J. W.; Ewing, D.** 2005. The development of large-scale structures in round impinging jets exiting long pipes at two Reynolds numbers, Experiments in Fluids 38(1): 50-58. https://doi.org/10.1007/800348-004-0883-2.
14. **Xu, Z.; Hang, H.** 2008.Scale boundary and inlet condition effects on impinging jets, Journal of Wind Engineering & Industrial Aerodynamics 96(12): 2383-2402. https://doi.org/10.1016/j.jweia.2008.04.002.
15. **Tummers, M .J.; Jacobse, J.** 2011. Voorbrood S. G. Turbulent flow in the near field of a round impinging jet, International Journal of Heat & Mass Transfer 54(23–24): 4939-4948. https://doi.org/10.1016/j.ijheatmasstransfer.2011.07.007.
16. **Tan, L.; Zhang, J.; Tan ,X. M.** 2006. Jet cooling impact value under nonuniform Crossflow, Aerospace Power 21(3): 528-532 (in China)
17. **Geng, L. P.; Zhou, J. P.; Li, W. J., Wang, Y. G., Yang, R**. 2012. Heat transfer and flow field characteristics under periodic turbulent jet impact, Acta Aerodynamica Sinica 30(4): 528-532 (in China).
18. **Wang, J.; Joseph, D. D.** 2006. Pressure corrections for the effects of viscosity on the irrotational flow outside Prandtl's boundary layer, Journal of Fluid Mechanics 557(557): 145-165.
19. **Ren, J.; Zhang, Y.; Shen, Z. F.** 2014. Numerical simulation of vane pump under non-designed condition based on modified RNG k-ε model, Ship Science and Technology 10: 101-105.
20. **Cai, N.; Xie, J.; Yu, X. L.** 2017. Rotation correction of K-ε model, China Equipment Engineering 1: 174-175 (in China).
21. **Židonis, I.** 2019. Curvilinear Stress-Strain Relationship for Concrete of EN-2 Regulation in the ZI Method and the Calculation of Beam Strength, Mechanika 25(5): 341-349. https://doi.org/10.5755/j01.mech.25.5.24453.
22. **Berber, A.** 2019. The effect of diesel-methanol blends with volumetric proportions on the performance and emissions of a diesel engine, Mechanika 25(5): 363-369. https://doi.org/10.5755/j01.mech.25.5.22954

Z. Wang, T. Wang, B. Zhang, H. W. Ma

SIMULATION STUDIES AND EXPERIMENTAL VERIFICATION OF THE TEST METHOD FOR INITIAL GUIDANCE THRUST

S u m m a r y

As one of the main actuators of the missile guidance control system, the steering gear can adjust the actual thrust and the deflection angle of the rudder surface through the closed-loop control system during the missile guidance process. The attitude correction and speed adjustment of the missile during flight can be accomplished by changing the output injection force by the electric steering gear. In this paper, the theoretical analysis of the jet thrust test mechanism was carried out by the unsteady turbulence analysis theory. Through the flow field simulation, the influence of the position of the bearing wall on the position of the recirculation zone of the impinging jet was studied, and the position of the bearing wall was determined, whose pressure value was closest to the true value. In addition, a simplified test system for jet thrust test was designed. The influence of wall position on the pressure value was verified by experiments, and the accuracy of the simulation results was verified.

Keywords: electric steering gear; load force; jet thrust; recirculation zone; flow field simulation.

Received May 29, 2019
Accepted October 14, 2020